

# Enhancing universal machine learning potentials with polarizable long-range interactions

Rongzhi Gao<sup>1</sup>, ChiYung Yam<sup>2,4</sup>, Jianjun Mao<sup>2</sup>, Shuguang Chen<sup>2,3</sup>, GuanHua Chen<sup>\*1,2</sup>, and Ziyang Hu<sup>†1,2</sup>

<sup>1</sup>Department of Chemistry, The University of Hong Kong, Pokfulam Road, Hong Kong SAR China

<sup>2</sup>Hong Kong Quantum AI Lab. Limited, Pak Shek Kok, Hong Kong SAR, China

<sup>3</sup>MattVerse Limited, Pak Shek Kok, Hong Kong SAR, China

<sup>4</sup>Shenzhen Institute for Advanced Study, University of Electronic Science and Technology of China, Shenzhen, China

October 18, 2024

## Abstract

Long-range interactions are crucial in determining the behavior of chemical systems in various environments. Accurate predictions of physical and chemical phenomena at the atomic level hinge on accurate modeling of these interactions. Here, we present a framework that substantially enhances the predictive power of machine learning interatomic potentials by incorporating explicit polarizable long-range interactions with an equivariant graph neural network short-range potential. The pretrained universal model, applicable across the entire periodic table, can achieve first-principles accuracy. This versatile model has been further applied to diverse areas of research, including the study of mechanical properties, ionic diffusivity in solid-state electrolytes, ferroelectricity, and interfacial reactions, demonstrating its broad applicability and robustness.

## Main

Molecular dynamics (MD) simulations are indispensable in describing different phenomena at the atomic level in disciplines such as chemistry, materials science, and biology<sup>1-4</sup>. While *ab initio* MD (AIMD)<sup>5</sup> simulation approaches offer unparalleled accuracy, their computational demands constrain their application to small timescales and length scales. On the other hand, classical MD (CMD)<sup>6,7</sup> simulations offer computational efficiency, but their accuracy is contingent upon empirical parameters. Machine learning interatomic potentials (MLIPs)<sup>8-11</sup> provide a solution that balances accuracy and computational efficiency, outperforming

traditional methods. In particular, MLIPs based on equivariant graph neural networks, such as NequIP<sup>12</sup>, DimeNet<sup>13</sup>, and MACE<sup>14</sup>, achieve excellent performance by introducing equivariant and invariant symmetries. Moreover, universal models trained on the periodic table such as M3GNet<sup>15</sup>, CHGNet<sup>16</sup>, and GNoME<sup>17</sup> have emerged, showing remarkable prospects for materials discovery.

While existing MLIPs with a cut-off of around 5 Å perform well in simulating interactions within localized chemical environments, they may fail to capture long-range phenomena. This hinders their ability to understand and elucidate the behaviors of complex materials<sup>18</sup>. These behaviors encompass electrostatic interactions, involving forces between charged particles, and dispersion terms, which arise from subtle fluctuations in electron distribution within molecules or atoms. Consequently, this limitation calls for further research and development to enhance the predictive capabilities of MLIPs across a wider range of distances and interactions. Various models have been proposed to address the challenges associated with long-range interactions. The third-generation<sup>19,20</sup> high-dimensional neural network potentials (HDNNPs) consider partial charges to be local properties, which could potentially be insufficient for describing systems with strong nonlocal dependencies in their electronic structures. To overcome this limitation, fourth-generation<sup>21,22</sup> HDNNPs were developed, incorporating the charge equilibration (QEq)<sup>23</sup> principles. In fourth-generation HDNNPs, partial charges are directly trained to match reference charges derived from first principles, resulting in qualitatively meaningful outcomes. This new approach has shown early success in addressing the shortcomings of the third generation.

The polarizable charge equilibration (PQEq)<sup>24-26</sup> method proposed by Naserifar et al. enhances the QEq method by

\*ghc@everest.hku.hk

†hzy@yangtze.hku.hk

incorporating polarization effects<sup>27,28</sup>. Unlike the fourth-generation HDNNPs and the conventional QEq scheme, PQEq uses quantum mechanics (QM) interaction energies instead of partial charges as targets for evaluating interatomic potentials. Notably, partial charges obtained from QM calculations are either derived from the direct partitioning of the molecular wave function into atomic contributions or calculated based on the analysis of physical observables. However, due to the incompleteness of basis sets and variances in the partitioning methods, properties calculated based on partial charges may not always be reliable<sup>16,24</sup>. Hence, substituting partial charges with the QM electrostatic interaction energies is expected to yield more general and widely applicable results. In previous works, there has been the development of PQEq parameters for 102 elements, derived from experimental data or high-level QM calculations<sup>23,29</sup>, and demonstrated its effectiveness in accurately reproducing QM electrostatic interaction energies<sup>24</sup>.

In this work, we introduce a novel framework that integrates the equivariant neural network potentials with the polarizable long-range electrostatic potentials. When combined with dispersion potentials, the pretrained universal model within this framework achieves accuracy comparable to first principles methods for elements in the periodic table up to Pu, while maintaining a low computational cost. Furthermore, we have applied this universal pretrained model across different areas of applications, including the predictions of mechanical properties of materials, phase transitions and hysteresis behaviors in ferroelectric materials, and interfacial reactions in solid-state batteries, thus leading to significant advancements in the fields of materials science and chemical simulation.

## Results

### Framework and performance

Our framework, which integrates short-range and long-range interactions is depicted in **Fig. 1a**. For a given chemical system and the boundary condition, our goal is to construct a mapping from atomic coordinates  $\mathbf{r}_i$  and atomic types  $z_i$  to the total potential energy  $E_{\text{pot}}$ . The potential energy is derived from second-order expansion<sup>24</sup> with respect to charge fluctuations and augmented by the dispersion term  $E_{\text{D3}}$ ,

$$E_{\text{pot}} = \sum_i \left( E_0^i(\mathbf{r}_i, z_i) + \chi_i^0 q_i + \frac{1}{2} \eta_i^0 q_i^2 + \frac{1}{2} K_s^i r_{ic}^2 \right) + \sum_{i>j} C_{ik,jl}(\mathbf{r}_{ik,jl}) q_{ik} q_{jl} + E_{\text{D3}}. \quad (1)$$

The zero-order atomic energy  $E_0^i$  corresponds to the short-range interactions of atom  $i$ , *i.e.*, the final layer scalar output

of the equivariant graph neural networks, while the higher-order self and interatomic Coulomb interactions represent the long-range electrostatic interactions. In the equivariant neural networks<sup>12</sup>, the initial features are generated using a trainable one-hot embedding that operates on the atomic types. The interatomic distance of atom  $i$  and atom  $j$ , denoted as  $|\mathbf{R}_{ij}|$ , is expanded by radial basis functions. Concurrently, the directional component of the interatomic vectors, expressed as  $\frac{\mathbf{R}_{ij}}{|\mathbf{R}_{ij}|}$ , is expanded by spherical harmonics functions. These features are utilized to construct the atomic graph. Then, through the equivariant message passing<sup>30</sup> schemes, the atomic features are updated. A multi-layer perceptron layer is then connected to derive the scalar output. To account for charge transfer and polarization effects, partial atomic charge  $q_i$  of atom  $i$  is contributed by the sum of the nuclear core charge  $q_{ic}$  and shell charge  $q_{is}$ , both of which assume a Gaussian charge distribution form. The first-order coefficients  $\chi^0$  are *electronegativities*, commonly defined as half of the sum of ionization potential (IP) and electron affinities (EA). The second-order coefficients  $\eta^0$  signifies *idempotential* or chemical hardness, defined as  $IP - EA$ . The spring constant  $K_s^i$  denotes the isotropic harmonic connectivity between the shell position  $\mathbf{r}_{is}$  and core position  $\mathbf{r}_{ic}$  of atom  $i$ . The Gaussian electrostatic energy is given by  $C(\mathbf{r}_{ik,jl}) q_{ik} q_{jl}$ , where  $i$  and  $j$  are the atomic indices, and  $k$  and  $l$  represent the core (*c*) or shell (*s*), respectively. In MD simulations, the partial charges are updated dynamically by minimizing the potential energy equation (**Eq. 1**) subject to the conservation of the net charge, and to the equality of chemical potentials for all atoms. The detailed derivation of PQEq and the response of the force to the external electric field can be found in the *Supplementary Information Part 1*. As our goal is to reproduce Density Functional Theory<sup>31</sup> (DFT) results, the DFT-D3 van der Waals dispersion energies correction<sup>32,33</sup> terms  $E_{\text{D3}}$  are employed to account for the dispersion. The forces on atoms  $\mathbf{F}_i$  and stress  $\sigma_{ab}$  on the cell can be calculated via auto differentiation of potential energy with respect to atomic coordinates and strain  $\epsilon_{ab}$ ,

$$\mathbf{F}_i = - \frac{\partial E_{\text{pot}}}{\partial \mathbf{r}_i} \quad (2)$$

$$\sigma_{ab} = \frac{1}{V_{\text{cell}}} \frac{\partial E_{\text{pot}}}{\partial \epsilon_{ab}}, \quad (3)$$

where  $V_{\text{cell}}$  denotes the cell volume.

We trained a universal model for all the periodic table elements up to Pu, as described in the **Methods** section, to evaluate the feasibility of this framework. Our results demonstrate mean absolute errors (MAE) of 18 meV per atom for energies  $E$ , 0.064 eV/Å for forces  $\mathbf{F}$ , and 0.301 GPa for stresses  $\mathbf{S}$  across a test set comprising 155,765 configurations. These results show a modest improvement compared to the previously established pretrained universal

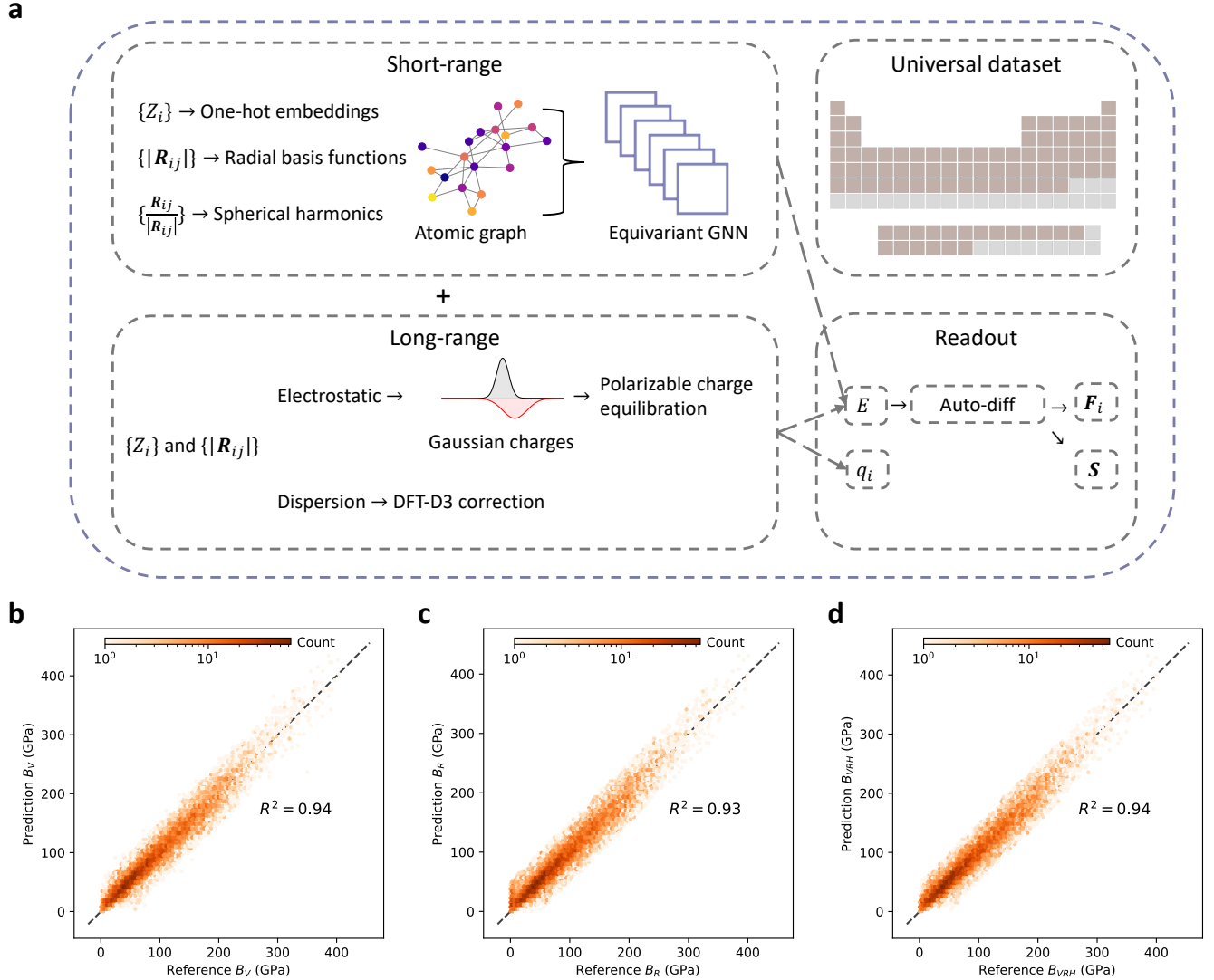


**Fig. 1: The architecture of the framework and model performance on bulk modulus.** **a**, The framework integrates short-range and long-range interactions, encompassing nearly the entire periodic table up to plutonium. Atomic number one-hot encoding, radial basis functions, and spherical harmonics are employed to construct the short-range atomic graph. This graph is then processed through an equivariant graph neural network to output the short-range energy. The lower part details the calculation of long-range interaction energy, which includes electrostatic and DFT-D3 dispersion terms. Each atom is represented by the Gaussian-type core and shell, enabling the calculation of electrostatic energy and partial charges through polarizable charge equilibration. The model can predict the forces and stresses by applying automatic differentiation to the total energy. Benchmarks on various calculation methods for the bulk modulus derived from first principles calculations and the model: **b**, Voigt approach, **c**, Reuss method, and **d**, Hill average.

model<sup>16</sup>, suggesting that incorporating long-range interactions enhances the accuracy of model in reproducing the outcomes predicted by DFT. To demonstrate the performance of the model, we conducted benchmarking using properties that were not labeled during the training process. First, we applied the pretrained model to predict the mechanical prop-

erties of 10,154 materials from the Materials Project<sup>35</sup>. **Fig. 1b-d** illustrate the comparison of the bulk modulus  $B$  determined by the pretrained model and DFT. Our pretrained model demonstrated impressive performance, achieving an  $R^2$  of 0.94 with the Voigt approach<sup>36</sup>  $B_V$  and Hill average method<sup>37</sup>  $B_{VRH}$ , and 0.93 using the Reuss method<sup>38</sup>

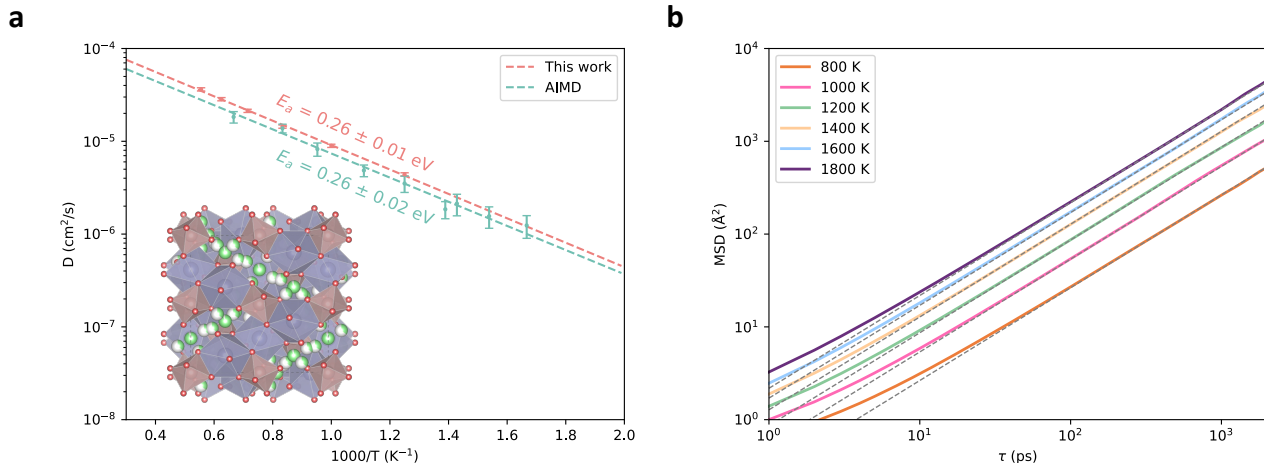


**Fig. 2: Li diffusivity in cubic phase  $\text{Li}_7\text{La}_3\text{Zr}_2\text{O}_{12}$ .** **a**, Crystal structure of  $\text{Ia}\bar{3}\text{d}$   $\text{Li}_7\text{La}_3\text{Zr}_2\text{O}_{12}$  and Arrhenius plots depicting the lithium-ion diffusion coefficients across varying temperatures. The dark blue polyhedron signifies La located at the 24(c) site and the light brown polyhedron indicates Zr at the 16(a) site. Li fraction occupies the 24(d) and 96(h) sites. Predicted diffusion coefficients of AIMD<sup>34</sup> and our model, complete with error bars, are presented to calculate activation energies. **b**, 2-ns mean square displacements of lithium-ion in c-LLZO with different temperatures ranging from 800 K to 1800 K in an increment of 200K. The linear dashed gray lines, with a slope of 1, are also plotted.

$B_R$ . These achievements not only highlight the robust performance of the model but also establish a solid foundation for the high-throughput screening of materials with exceptional mechanical properties.

## Li diffusion in solid-state electrolytes

Next, we simulate the kinetic transport properties of a solid-state electrolyte to demonstrate the capability of our model to reproduce results from AIMD simulations. Specifically, we investigated lithium-ion diffusivity within the cubic phase of  $\text{Li}_7\text{La}_3\text{Zr}_2\text{O}_{12}$  (c-LLZO)<sup>39</sup>, a crystalline superionic conductor known for its remarkable stability as a lithium conductor. Owing to the efficiency of our pretrained model, we are able to conduct MD simulations on the c-LLZO comprising 64 formula units, with a duration of 2 ns for each temperature range from 800 K to 1800K. **Fig. 2a** presents the Arrhenius plots derived from our model and AIMD<sup>34</sup> simulations. The diffusion coefficients were determined from the slope of the logarithmic mean square displacements (MSD) versus logarithmic time within the Fickian regime<sup>40</sup>, as depicted in **Fig. 2b**. Compared to previous work using AIMD, our model clearly reproduces the diffusion coefficients and activation energy of c-LLZO. More importantly, with the ability to reach larger model sizes and longer simulation times, our model achieves these results with significantly reduced error. This capability not only delivers comparable results to AIMD simulations but also enables larger-scale simulations that cannot be assessed by AIMD simulations, enhanc-

ing the statistical significance of MD studies. Consequently, the framework developed in this work provides more reliable and comprehensive data for diffusion analysis in solid-state electrolytes.

## Polarization and ferroelectricity

To verify the ability of our model to handle polarized systems, we performed MD simulations on a typical perovskite ferroelectric material  $\text{BaTiO}_3$ . As temperature increases,  $\text{BaTiO}_3$  undergoes a non-trivial phase transition process<sup>41</sup>. Below 183 K, it adopts a rhombohedral structure with local polarization along the [111] direction. As the temperature rises, it transitions to an orthorhombic phase with polarization along the [110] direction, then to a tetragonal phase with polarization along [100] direction at 278 K. Finally, at 403 K, it converts to a cubic paraelectric phase. Accurately simulating phase changes in ferroelectric substances requires precise potential energy functions that can respond to the small atomic shifts and structural changes, as well as account for the free energy surfaces under the conditions of finite-temperature thermodynamics<sup>42</sup>. The rhombohedral-orthorhombic-tetragonal-cubic phase sequence of  $\text{BaTiO}_3$  has been extensively studied and reproduced using effective Hamiltonians<sup>43,44</sup>, CMD<sup>45,46</sup>, and specialized MLIPs models<sup>42,47</sup>.

To detect subtle lattice distortions and variations in free energy that distinguish different phases, a  $10 \times 10 \times 10$  supercell of  $\text{BaTiO}_3$  was simulated. This allowed for a detailed

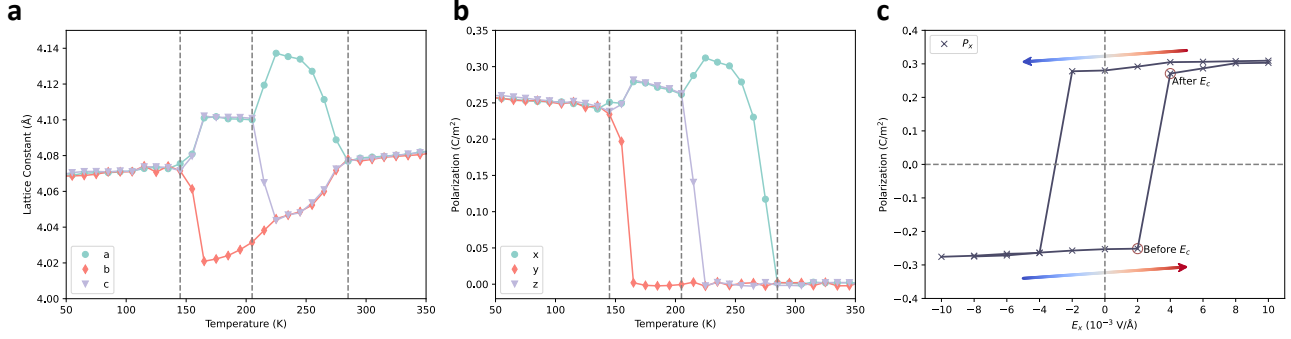


**Fig. 3: The phase transitions and  $P$ - $E$  loop of  $\text{BaTiO}_3$ .** The temperature dependence of **a**, lattice constants, and **b**, local polarizations of unit cells exhibit notable changes during the phase transitions observed from MD simulations on  $10 \times 10 \times 10$   $\text{BaTiO}_3$ . **c**,  $P$ - $E$  loop of  $20 \times 10 \times 10$  tetragonal  $\text{BaTiO}_3$  at 235 K. The electric field is applied along the  $x$ -direction.

analysis of the structural changes that occurred between different phases, providing valuable insights into the properties of materials. **Fig. 3a** and **b** illustrate the simulation results, which clearly identify four distinct phases and the three first-order phase transitions within the simulated temperature range. Below 145 K, the overall average polarization of the supercell aligns with the [111] direction, indicative of the rhombohedral phase. At 145 K, a phase transition to orthorhombic is suggested as the  $y$ -component of polarization approaches zero. With further increase to 205 K, the polarization predominantly orients along the  $x$ -direction, indicating the tetragonal phase. This phase persists until 285 K, where the cubic paraelectric phase is observed. The obtained phase transition temperatures align closely with those predicted by various models and experiments, as shown in **Table 1**. Notably, utilizing first principles methods or fitting potential energy surfaces to first principles data often underestimates these temperatures, which is attributed to the approximated exchange-correlation functional<sup>45</sup> employed in DFT. Although the predicted phase transition temperatures are lower than the experimentally observed values, the model effectively captures the sequence of phase transitions as measured in experiments, demonstrating the efficacy of the pre-trained universal model in modeling highly polarized phase transitions in ferroelectric materials. In addition, we investigated the response to external electric fields, focusing specifically on the hysteresis behavior of  $\text{BaTiO}_3$ . By applying varying electric fields, we can chart the polarization-electric field hysteresis loop ( $P$ - $E$  loop). Experimental studies have shown that the critical thickness of  $\text{BaTiO}_3$  for ferroelectricity is about 4.8 nm<sup>48</sup>. To clearly illustrate the ferroelectric phenomenon, we employed a supercell of  $20 \times 10 \times 10$  tetragonal  $\text{BaTiO}_3$  ( $\sim 8.2$  nm along  $a$ -direction) to simulate the  $P$ - $E$  loop at 235 K. The electric field was applied along the  $x$ -direction, and the resulting changes in the  $x$ -component local polarization of the unit cell are depicted

in **Fig. 3c**. The hysteresis loop obtained from our simulation reveals that the coercive electric field  $E_c$  is about 300 kV/cm. This finding is consistent with experimental measurement of thin film  $\text{BaTiO}_3$ <sup>49,50</sup> and effective Hamiltonian calculations<sup>51</sup>, both of which report values ranging from 200-500 kV/cm. Our universal model excels in temperature-dependence phase transitions and responses to external electric fields in ferroelectric materials. This proficiency holds significant promise for exploring ferroelectric characteristics, which are crucial for the development of non-volatile memory devices, transducers, microsensors, and capacitors.

**Table 1: Comparison of  $\text{BaTiO}_3$  phase transition temperatures obtained by different methods and experiments.**

Method	$T_{c,R-O}$ (K)	$T_{c,O-T}$ (K)	$T_{c,T-C}$ (K)
This work	145	205	285
First Principles <sup>52</sup>	$150 \pm 10$	$195 \pm 5$	$265 \pm 5$
Second Principles <sup>53</sup>	140	180	224
Effective Hamiltonian <sup>44</sup>	119	158	257
ReaxFF <sup>54</sup>	N.A.	N.A.	240
MLIPs <sup>42</sup>	18.6	91.4	182.4
Experiments <sup>55</sup>	183	278	403

## Interface formation of lithium thiophosphates

The final application studied in this work involves all-solid-state batteries, which represent a breakthrough in the evolution of next-generation energy solutions, owing to their superior energy density and inherent safety features<sup>56</sup>. Lithium thiophosphate, known for its exceptional ionic conductivity ( $\sim 10^{-3}$  S/cm), is deemed the most promising candidate for solid electrolytes and has been widely studied through experiments<sup>57-59</sup> and computer modelings<sup>60-62</sup>. Notably, the nanoporous  $\beta$ - $\text{Li}_3\text{PS}_4$  has been validated to exhibit outstanding cycling stability<sup>63</sup>, presumably attributed to the for-

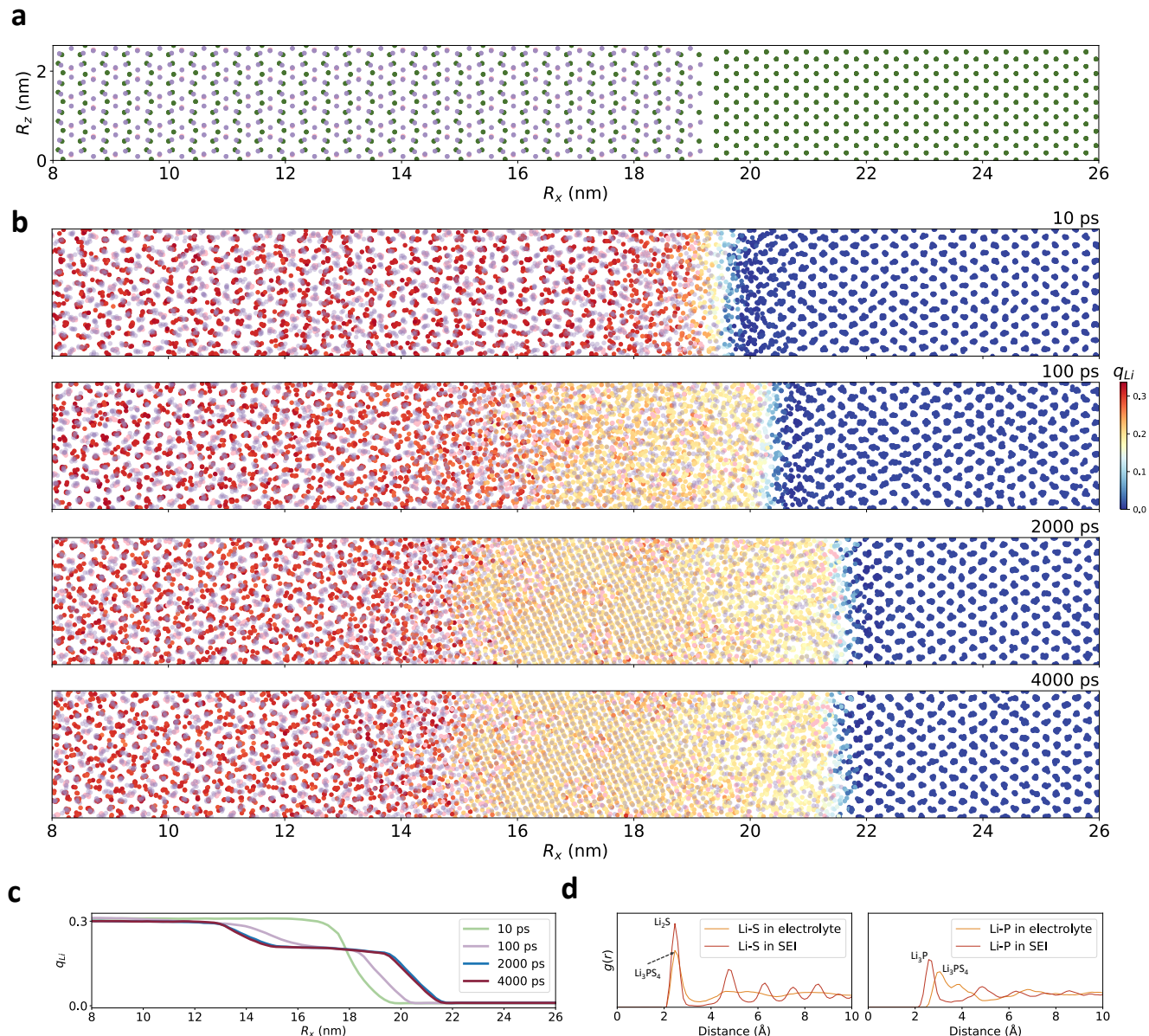


**Fig. 4: The formation of the lithium thiophosphates and lithium metal SEI layer at 300 K and 1 atm.** **a**, The initial structure of  $\beta - \text{Li}_3\text{PS}_4$  (010)/Li (001) interface. The elements are color-coded: Li in green, S in purple, and P in pink. A segment of the primary reaction zone, ranging from 8 to 26 nanometers is displayed. **b**, Snapshots at different times during the MD simulations. The partial charges on lithium ions are represented with color coding to enhance the visibility of structural transformations during the formation of SEI. The SEI layer, approximately 8.5 nm in thickness, forms after 4 ns MD simulations, comprising an amorphous  $\beta - \text{Li}_3\text{PS}_4/\text{Li}_2\text{S}$  interface ( $\sim 2$  nm), a crystalline  $\text{Li}_2\text{S}$  layer ( $\sim 4.5$  nm), and an amorphous  $\text{Li}_2\text{S}$  ( $\text{Li}_3\text{P}$ )/Li interface layer ( $\sim 2$  nm) in sequence. **c**, The distributions of the Li partial atomic charges along the  $x$ -direction at 10, 100, 2000, and 4000 ps. **d**, The radial distribution function plots of Li-S and Li-P within the electrolyte and SEI layer.

mation of  $\text{Li}_2\text{S}$  and  $\text{Li}_3\text{P}$  solid-electrolyte interphases (SEI) during the initial battery cycles, which serves to passivate further degradation of the electrolyte<sup>61,64–66</sup>. To investigate the formation of SEI, we utilized the pretrained universal

model to simulate the interfacial MD of the solid electrolyte  $\beta - \text{Li}_3\text{PS}_4$  in contact with the lithium metal anode, encompassing a system of 13,760 atoms.

The initial  $\beta - \text{Li}_3\text{PS}_4/\text{Li}$  interfacial structure, measuring

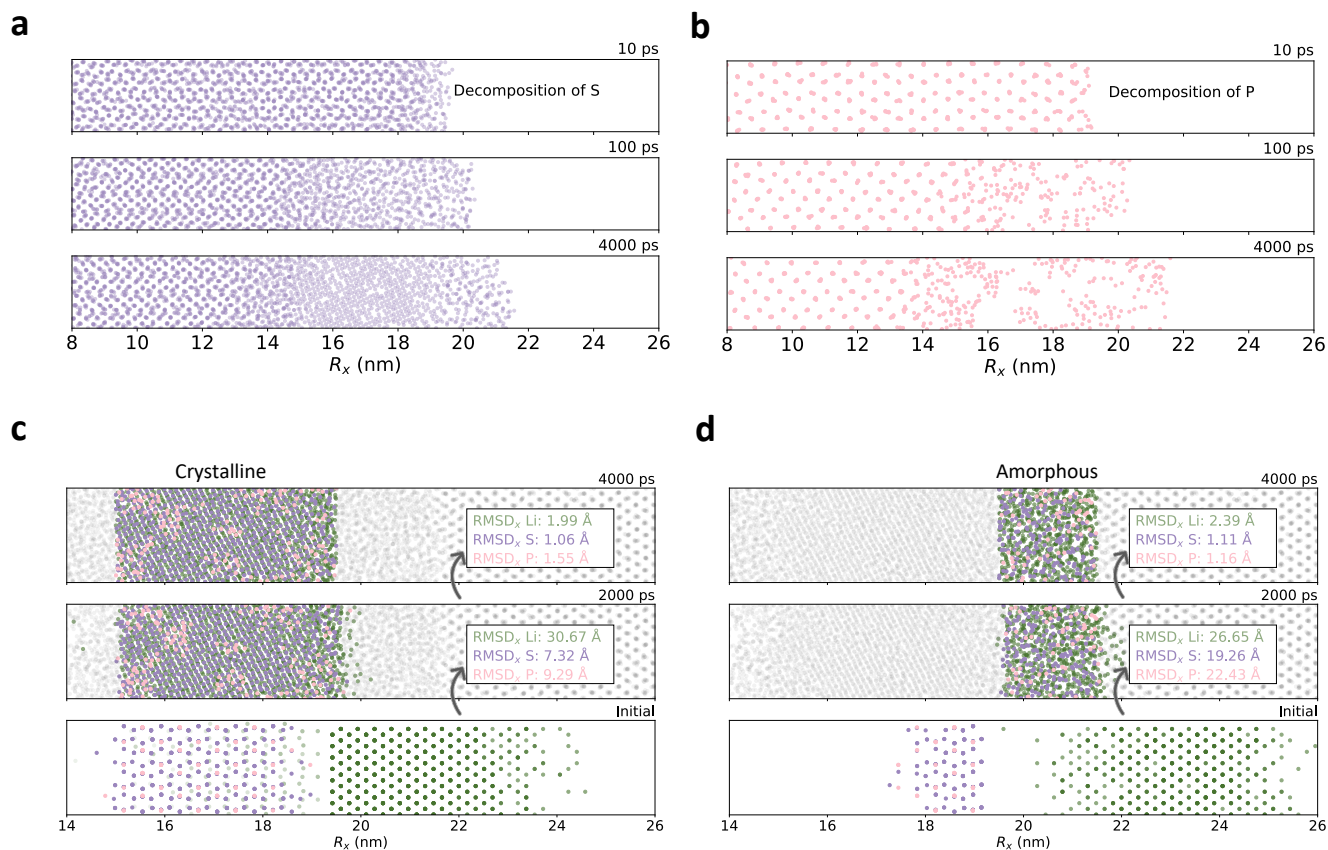


**Fig. 5: The decomposition dynamics of  $\text{Li}_3\text{PS}_4$  electrolyte and component analyses of SEI.** The snapshots capture the dynamic decomposition behavior of  $\text{PS}_4$ , showcasing: **a**, the sulfur, and **b**, the phosphorus component. To elucidate the formation mechanism of the SEI layer, atomic component analyses of the **c**, crystalline, and **d**, amorphous  $\text{Li}_2\text{S}$  regions are compared among 4-ns (upper), 2-ns (middle), and the initial state (lower). The elements are color-coded: Li in green, S in purple, and P in pink. The  $x$ -component root mean squared displacements ( $\text{RMSD}_x$ ) of Li, P, and S between the initial and the 2-ns states and between 4-ns and 2-ns states are also shown.

33.15 nm  $\times$  3.1 nm  $\times$  2.6 nm, was utilized in the MD simulations, as depicted in **Fig. 4a**. The highly reactive Li metal began to interact with  $\text{PS}_4$  tetrahedron at the interface, triggering the formation of the SEI layer as illustrated in **Fig. 4b**. With the growth of the SEI layer, electrons were transferred from the Li anode to the  $\text{Li}_3\text{PS}_4$  electrolyte, which causes a gradual increase of the partial charges of Li as they migrate from the anode, across the SEI, and into the electrolyte. This results in a transition from metal lithium to ions. The dynamic behavior of partial charges at the anode-electrolyte interface is a critical aspect showcased in **Fig. 4c**. Initially, at 10 ps, the partial charges of lithium changed almost linearly from the anode to the electrolyte. Over time, this distribution evolved and showed a distinct plateau at 100 ps. This phenomenon could be attributed to the ordered structuring of the SEI, signifying the nucleation of crystalline structures. Ultimately, a stable lithium partial charges plateau was

formed between the anode and the electrolyte, spanning a range of 15 to 19.5 nm. This is further supported by the visualized structure depicted in **Fig. 4b**, where the plateau within the SEI aligns with the  $\text{Li}_2\text{S}$  crystal region. Chen *et al.*<sup>60</sup> employed AIMD simulations to investigate the radial distribution functions (RDF) of Li-P and Li-S bonds, which concluded that the decompositions of electrolytes in lithium thiophosphates are primarily due to the decomposition of  $\text{PS}_4$  tetrahedron by the active lithium metal, leading to the formation of new Li-P and Li-S bonds. Our RDF analysis confirmed the formation of Li-S and Li-P bonds within the SEI and electrolyte as depicted in **Fig. 4d**. In agreement with the AIMD simulations<sup>60</sup>, we observed the emergence of a new Li-P peak within the SEI at approximately 2.5 Å. Furthermore, within the SEI, the Li-S bond displayed RDF characteristics consistent with crystalline  $\text{Li}_2\text{S}$ <sup>67</sup>. For the Li-P bonds, the peak shape closely resembles that of amorphous

Li<sub>3</sub>P AIMD simulations<sup>68</sup>. As illustrated in **Fig. 5a** and **b**, the ultimate decomposition products of P form only short-range ordered structures, in contrast to S, which forms long-range ordered structures. This observation agrees with the measurements where Li<sub>2</sub>S crystals were detected but Li<sub>3</sub>P crystals were absent in cryogenic transmission electron microscopy (cryo-TEM) experiments, as noted in reference<sup>58</sup>. To enhance the understanding of the formation mechanism, the atomic compositions of the SEI in both crystalline and amorphous Li<sub>2</sub>S regions were examined. As depicted in **Fig. 5c** and **d**, within the first 2 ns, the emergence of amorphous Li<sub>2</sub>S and Li<sub>3</sub>P regions was attributed to the swift diffusion of P and S atoms. Conversely, the formation of crystalline Li<sub>2</sub>S regions was predominantly influenced by the swift diffusion of Li atoms and slower diffusion of P and S atoms. As the system further evolves to 4 ns, the diffusions slow down, which also confirmed that the formation of crystalline Li<sub>2</sub>S region hindered further atomic diffusion and thus slowed the growth of the SEI. As illustrated in **Fig. 4b**, during the initial phase of decomposition (10-100 ps), the swift diffusion of P, S, and Li led to the formation of an interface of about 3 nm thick. However, in a later stage between 100 and 2000 ps, the formation of Li<sub>2</sub>S nuclei impeded the diffusion of P and S atoms, resulting in a period of sluggish SEI growth. Consequently, the interface experienced only a slight expansion in this period, increasing by only 1 nm. Furthermore, in the following 2 ns, there was essentially no SEI growth. The final interface structure ( $\sim 8.5$  nm) could be characterized by a 4.5 nm crystalline Li<sub>2</sub>S region sandwiched between two 2-nm transitional layers. The cessation of growth at this interface suggests that the crystalline Li<sub>2</sub>S and amorphous Li<sub>3</sub>P within the crystal region contribute to the stabilization of both the lithium metal anode and the electrolyte, which agrees with the theoretical predictions made by DFT calculations<sup>64</sup>. Additionally, we studied the interface reactions between Li<sub>6</sub>PS<sub>5</sub>Cl and lithium metal, as detailed in *Supplementary Information Part 4*. As shown in **Fig. S1**, at a pressure of 1 atm and temperature of 300 K, Li<sub>6</sub>PS<sub>5</sub>Cl formed an interface of about 5-nm thick after 2 ns. This indicates that the Li<sub>6</sub>PS<sub>5</sub>Cl electrolyte exhibits a higher stability against lithium metal at room temperature compared to Li<sub>3</sub>PS<sub>4</sub>. Upon elevating the temperature to 500 K, polycrystalline Li<sub>2</sub>S was detected, in agreement with cryo-TEM observations<sup>58</sup>.

The above molecular dynamics simulations highlight the superiority of our pretrained model in describing the interfacial reactions, which will significantly advance the development of future all-solid-state battery applications. This approach allows for a detailed examination of the interactions and behaviors at the atomic level. Through these simulations, valuable insights can be gained into the dynamic interactions that govern the stability and performance of all-solid-state batteries.

## Discussion

In this study, we introduced a novel framework that integrates short-range equivariant machine learning interatomic potentials with long-range polarizable interactions. This framework enhances the precision of long-range interactions by dynamically minimizing potential energy with respect to charge fluctuations, effectively incorporating charge transfer and polarization effects. By utilizing electrostatic interaction energy directly instead of relying on partial charges, the proposed framework facilitates the development of a universal model with broad applicability. The robustness of the model is further demonstrated through benchmarking of mechanical properties, specifically the prediction of bulk modulus across a large dataset of materials. The high  $R^2$  values achieved indicate reliability of the model in predicting material properties that were not explicitly included in the training process. This capability is essential for high-throughput screening, potentially accelerating the discovery of materials with exceptional mechanical properties. In addition, the model has been successfully applied to study dynamic properties, such as lithium-ion diffusion in solid-state electrolytes and phase transitions in ferroelectric materials. Its ability to replicate AIMD simulations, while significantly reducing computational costs, suggests that it could be a valuable tool for investigating kinetic properties across a wide range of materials. Moreover, the simulations of temperature-dependence phase transition of ferroelectric material BaTiO<sub>3</sub>, as well as its  $P$ - $E$  loop confirmed the capability of the model in addressing polarizable systems. Regarding the interfacial reactions between lithium thiophosphate electrolytes and lithium metal anodes in solid-state batteries, the model successfully elucidated the mechanism of interface formation and its impact on battery performance, highlighting its potential for realistic-scale simulations.

In conclusion, the pretrained universal model presented in this work not only delivers commendable performance across various domains but also establishes a solid foundation for future high-throughput material screening and a deeper understanding of material behaviors. This model unlocks invaluable insights that have the potential to propel the development of a new generation of high-performance materials and transformative energy solutions. The implications of this work are far-reaching and significantly enhance our technological capabilities.

## Methods

### Dataset

To train a universal equivariance neural network potential, we used the MPtrj Dataset<sup>16</sup> sourced from Materials Projects<sup>35</sup> as the pretraining dataset. All configura-



tions were calculated using DFT with the PBE<sup>69</sup>/PBE+U<sup>70</sup> exchange-correlation functional and pseudopotential basis. The PBE/PBE+U mixing compatibility correction<sup>71</sup> was applied to ensure energy consistency. After removing unreasonable configurations, the dataset comprised a total of 1,557,645 material configurations, each with corresponding energies, forces, and stresses.

## Model training

The higher-order energy terms and the electrostatic Coulomb interaction energies due to charge fluctuations should be deducted from the total potential energy. Appropriately setting the PQEq parameters is crucial for training a universal framework. In particular, the Li parameters were refitted to reproduce the electrostatic interaction energies observed in QM. Detailed information on the fitting process and the PQEq parameters used in this work can be found in the *Supplementary Information Part 2*.

For equivariant neural network training, the NequIP<sup>12</sup> model was utilized, incorporating six equivariant layers with node features set at  $256 \times 0e + 256 \times 1e$ . Spherical harmonic basis functions were used to represent interatomic directions, denoted as  $1 \times 0e + 1 \times 1o$ . Interatomic distances were described using eight Bessel basis functions, and a cut-off value of 5.0 Å was chosen for building the short-range neighbor list. The dataset is divided into training set, validation set, and test set in a ratio of 6:1:1.

The total loss function ( $\mathcal{L}$ ) of prediction values  $\mathbf{x}^{\text{pred}}$  and reference first principles values  $\mathbf{x}^{\text{ref}}$  can be expressed as,

$$L(\mathbf{x}^{\text{pred}}, \mathbf{x}^{\text{ref}}) = \sum_{i=1}^N \frac{1}{N} (\mathbf{x}_i^{\text{pred}} - \mathbf{x}_i^{\text{ref}})^2 \quad (4)$$

$$\mathcal{L} = \omega_E \cdot L(\mathbf{E}^{\text{pred}}, \mathbf{E}^{\text{ref}}) + \omega_F \cdot L(\mathbf{F}^{\text{pred}}, \mathbf{F}^{\text{ref}}) + \omega_S \cdot L(\mathbf{S}^{\text{pred}}, \mathbf{S}^{\text{ref}}), \quad (5)$$

where energies  $\mathbf{E}$ , forces  $\mathbf{F}$  and stresses  $\mathbf{S}$  weights were set as  $\omega_E = 1$ ,  $\omega_F = 10$ , and  $\omega_S = 10$  with quantity units of eV, eV/Å, and eV/Å<sup>3</sup>. The batch size was selected as 128, and the Adam optimizer was employed with an initial learning rate of  $10_{-3}$ . A total of 71,452,040 trainable parameters were initialized with the random seed 3407. The implementation of the entire neural networks and long-range interactions was based on JAX 0.4.20<sup>72</sup>. The training was conducted on a single NVIDIA H100-PCIe GPU, utilizing CUDA version 12.3 and Driver version 545.23.06.

## Dynamics

The Atomic Simulation Environment (ASE)<sup>73</sup> was utilized as the interface for geometry relaxations and MD simulations. Structure relaxations were conducted using the

limited-memory BFGS<sup>74</sup> method. Both atomic coordinates and cell vectors were optimized concurrently until the forces fell below the convergence threshold of 0.05 eV/Å.

The c-LLZO with a space group of Ia $\bar{3}$ d originated from experimental structures detailed in reference<sup>39</sup>. The structure was expanded to a 2×2×2 supercell. Subsequently, 180 lithium atoms were randomly placed on the 24(d) sites, and an additional 268 lithium atoms on the 96(h) sites. After relaxation, the structure served as the starting point for MD simulations. The isothermal isobaric (NpT) ensemble simulations were performed with the temperature control via Nosé-Hoover thermostat<sup>75,76</sup> and pressure maintained at 1 atm using Parrinello-Rahman barostat<sup>77,78</sup> to determine the lattice constants at various temperatures. Then, the canonical (NVT) ensemble simulations with the Nosé-Hoover thermostat were utilized to ascertain the lithium diffusion properties within c-LLZO. A time step of 2 fs was used for all NpT and NVT simulations. In the case of NVT simulations, following a 100 ps equilibration period, 2-ns trajectories' mean squared displacements of Li ions were employed to calculate the self-diffusion coefficients at various target temperatures. Additionally, we conducted an uncertainty analysis of the diffusion coefficients, applying the empirical error estimation method as detailed in reference<sup>34</sup>.

To construct the phase diagram of the BaTiO<sub>3</sub> crystal structure, a supercell consisting of a 10×10×10 R $\bar{3}$ m BaTiO<sub>3</sub> lattice with 5000 atoms was created. The crystal structure data for BaTiO<sub>3</sub> was sourced from the Materials Project<sup>35</sup>. NpT simulations with the Nosé-Hoover thermostat and Parrinello-Rahman barostat were performed with a 1-fs timestep. Throughout the simulations, the pressure was consistently maintained at 1 atmosphere. To regulate temperature, the procedure began at 5 K and involved incrementing the temperature by 10 K every 20 ps. The average lattice constants and the local polarization of the unit cell, denoted as  $\mathbf{P}_u$ , were determined using data from the final 10 ps of trajectories at each temperature step. For the comprehensive calculation method of the local polarization, please refer to the *Supplementary Information Part 3*. To obtain the local polarization-electric field hysteresis loop of BaTiO<sub>3</sub>, the average structures of the 235 K tetragonal phase were utilized. NpT MD simulations were conducted on the 20×10×10 supercell of the tetragonal BaTiO<sub>3</sub>, comprising 10,000 atoms, to derive the  $P$ - $E$  loop. Electric fields ranging from  $1 \times 10^{-2}$  V/Å to  $-1 \times 10^{-2}$  V/Å were applied along the  $x$ -direction and then reversed back to  $1 \times 10^{-2}$  V/Å.

We utilized a 13760-atom structure consisting of a ca. 13.6-nm thick Im $\bar{3}$ m lithium metal anode with [100] facet, paired with a ca. 19.1 nm thick Pnma  $\beta$  - Li<sub>3</sub>PS<sub>4</sub> electrolyte with [010] facet to illustrate the SEI formation across realistic spatial and temporal scales. The system was structured with periodic lateral dimensions measuring 3.1 nm by 2.6 nm. The unit cell of anode and electrolyte structures

originated from the Materials Project<sup>35</sup>. The entire cell was subject to periodic boundary conditions, with a 1 nm atomic layer fixed on each side along the  $x$ -direction to ensure a singular interface reaction. NpT MD simulations were conducted at a standard temperature of 300 K and a pressure of 1 atm by Nosé-Hoover thermostat and Parrinello-Rahman barostat with a timestep of 2 fs. Initial velocities for the particles were assigned randomly following the Maxwell-Boltzmann distribution, and the simulations were carried out for a duration of 4 ns.

## Data availability

Source data will be provided with this paper. The dataset is accessible through the Materials Project<sup>16,35</sup>. Detailed PQEq parameters are provided in the Supplementary Information.

## Code availability

The NequIP<sup>12</sup> code originated from the open-source project `jax-md`<sup>79</sup>. The JAX implementation of PQEq and DFT-D3 will be made available at <https://github.com/reaxnet/jax-nb>.

## References

- [1] Martin Karplus and Gregory A Petsko. Molecular dynamics simulations in biology. *Nature*, 347(6294):631–639, 1990.
- [2] Thomas P Senftle, Sungwook Hong, Md Mahbulul Islam, Sudhir B Kylasa, Yuanxia Zheng, Yun Kyung Shin, Chad Junkermeier, Roman Engel-Herbert, Michael J Janik, Hasan Metin Aktulga, et al. The ReaxFF reactive force-field: development, applications and future directions. *npj Computational Materials*, 2(1):1–14, 2016.
- [3] Nan Yao, Xiang Chen, Zhong-Heng Fu, and Qiang Zhang. Applying classical, *ab initio*, and machine-learning molecular dynamics simulations to the liquid electrolyte for rechargeable batteries. *Chemical Reviews*, 122(12):10970–11021, 2022.
- [4] Peng-Jui Chen, Alexander Q Cusumano, Kaylin N Flesch, Christian Santiago Strong, William A Goddard III, and Brian M Stoltz. Molecular dynamics investigations of dienoate [4+ 2] reactions. *Journal of the American Chemical Society*, 146(18):12758–12765, 2024.
- [5] Radu Iftimie, Peter Minary, and Mark E Tuckerman. *Ab initio* molecular dynamics: Concepts, recent developments, and future trends. *Proceedings of the National Academy of Sciences*, 102(19):6654–6659, 2005.
- [6] Anthony K Rappé, Carla J Casewit, KS Colwell, William A Goddard III, and W Mason Skiff. UFF, a full periodic table force field for molecular mechanics and molecular dynamics simulations. *Journal of the American chemical society*, 114(25):10024–10035, 1992.
- [7] Adri CT Van Duin, Siddharth Dasgupta, Francois Lorant, and William A Goddard. ReaxFF: a reactive force field for hydrocarbons. *The Journal of Physical Chemistry A*, 105(41):9396–9409, 2001.
- [8] Kristof Schütt, Pieter-Jan Kindermans, Huziel Enoc Saucedo Felix, Stefan Chmiela, Alexandre Tkatchenko, and Klaus-Robert Müller. Schnet: A continuous-filter convolutional neural network for modeling quantum interactions. *Advances in neural information processing systems*, 30, 2017.
- [9] Kristof Schütt, Oliver Unke, and Michael Gastegger. Equivariant message passing for the prediction of tensorial properties and molecular spectra. pages 9377–9388, 2021.
- [10] Jörg Behler and Michele Parrinello. Generalized neural-network representation of high-dimensional potential-energy surfaces. *Physical review letters*, 98(14):146401, 2007.
- [11] Linfeng Zhang, Jiequn Han, Han Wang, Roberto Car, and Weinan E. Deep potential molecular dynamics: a scalable model with the accuracy of quantum mechanics. *Physical review letters*, 120(14):143001, 2018.
- [12] Simon Batzner, Albert Musaelian, Lixin Sun, Mario Geiger, Jonathan P Mailoa, Mordechai Kornbluth, Nicola Molinari, Tess E Smidt, and Boris Kozinsky. E (3)-equivariant graph neural networks for data-efficient and accurate interatomic potentials. *Nature communications*, 13(1):2453, 2022.
- [13] Johannes Gastegger, Janek Groß, and Stephan Günnemann. Directional message passing for molecular graphs. *arXiv preprint arXiv:2003.03123*, 2020.
- [14] Ilyes Batatia, David P Kovacs, Gregor Simm, Christoph Ortner, and Gábor Csányi. MACE: Higher order equivariant message passing neural networks for fast and accurate force fields. *Advances in Neural Information Processing Systems*, 35:11423–11436, 2022.
- [15] Chi Chen and Shyue Ping Ong. A universal graph deep learning interatomic potential for the periodic table. *Nature Computational Science*, 2(11):718–728, 2022.
- [16] Bowen Deng, Peichen Zhong, KyuJung Jun, Janosh Riebesell, Kevin Han, Christopher J Bartel, and Gerbrand Ceder. CHGNet as a pretrained universal neural network potential for charge-informed atomistic modelling. *Nature Machine Intelligence*, 5(9):1031–1041, 2023.
- [17] Amil Merchant, Simon Batzner, Samuel S Schoenholz, Muratahan Aykol, Gowoon Cheon, and Ekin Dogus Cubuk. Scaling deep learning for materials discovery. *Nature*, 624(7990):80–85, 2023.
- [18] Dylan M Anstine and Olexandr Isayev. Machine learning interatomic potentials and long-range physics. *The Journal of Physical Chemistry A*, 127(11):2417–2431, 2023.
- [19] Nongnuch Artrith, Tobias Morawietz, and Jörg Behler. High-dimensional neural-network potentials for multicomponent systems: Applications to zinc oxide. *Physical Review B—Condensed Matter and Materials Physics*, 83(15):153101, 2011.
- [20] Tobias Morawietz, Vikas Sharma, and Jörg Behler. A neural network potential-energy surface for the water dimer based on environment-dependent atomic energies and charges. *The Journal of chemical physics*, 136(6), 2012.
- [21] Jörg Behler. Four generations of high-dimensional neural network potentials. *Chemical Reviews*, 121(16):10037–10072,

- 2021.
- [22] Tsz Wai Ko, Jonas A Finkler, Stefan Goedecker, and Jörg Behler. A fourth-generation high-dimensional neural network potential with accurate electrostatics including non-local charge transfer. *Nature communications*, 12(1):398, 2021.
- [23] Anthony K Rappe and William A Goddard III. Charge equilibration for molecular dynamics simulations. *The Journal of Physical Chemistry*, 95(8):3358–3363, 1991.
- [24] Saber Naserifar, Daniel J Brooks, William A Goddard, and Vaclav Cvicek. Polarizable charge equilibration model for predicting accurate electrostatic interactions in molecules and solids. *The Journal of chemical physics*, 146(12), 2017.
- [25] Soonho Kwon, Saber Naserifar, Hyuck Mo Lee, and William A Goddard III. Polarizable charge equilibration model for transition-metal elements. *The Journal of Physical Chemistry A*, 122(48):9350–9358, 2018.
- [26] Julius J Oppenheim, Saber Naserifar, and William A Goddard III. Extension of the polarizable charge equilibration model to higher oxidation states with applications to Ge, As, Se, Br, Sn, Sb, Te, I, Pb, Bi, Po, and At elements. *The Journal of Physical Chemistry A*, 122(2):639–645, 2017.
- [27] Moon Young Yang, Omar O’Mari, William A Goddard III, and Valentine I Vullev. How permanent are the permanent macrodipoles of anthranilamide bioinspired molecular electrets? *Journal of the American Chemical Society*, 146(8):5162–5172, 2024.
- [28] Saber Naserifar, Yalu Chen, Soonho Kwon, Hai Xiao, and William A Goddard. Artificial intelligence and QM/MM with a polarizable reactive force field for next-generation electrocatalysts. *Matter*, 4(1):195–216, 2021.
- [29] David R Lide and HPR Frederikse. CRC handbook of chemistry and physics, CRC press. *Inc, Boca Raton, FL*, 1995.
- [30] Justin Gilmer, Samuel S Schoenholz, Patrick F Riley, Oriol Vinyals, and George E Dahl. Neural message passing for quantum chemistry. pages 1263–1272, 2017.
- [31] Walter Kohn and Lu Jeu Sham. Self-consistent equations including exchange and correlation effects. *Physical review*, 140(4A):A1133, 1965.
- [32] Stefan Grimme, Jens Antony, Stephan Ehrlich, and Helge Krieg. A consistent and accurate *ab initio* parametrization of density functional dispersion correction (DFT-D) for the 94 elements H-Pu. *The Journal of chemical physics*, 132(15), 2010.
- [33] Stefan Grimme, Stephan Ehrlich, and Lars Goerigk. Effect of the damping function in dispersion corrected density functional theory. *Journal of computational chemistry*, 32(7):1456–1465, 2011.
- [34] Xingfeng He, Yizhou Zhu, Alexander Epstein, and Yifei Mo. Statistical variances of diffusional properties from *ab initio* molecular dynamics simulations. *npj Computational Materials*, 4(1):18, 2018.
- [35] Anubhav Jain, Shyue Ping Ong, Geoffroy Hautier, Wei Chen, William Davidson Richards, Stephen Dacek, Shreyas Cholia, Dan Gunter, David Skinner, Gerbrand Ceder, et al. Commentary: The Materials Project: A materials genome approach to accelerating materials innovation. *APL materials*, 1(1), 2013.
- [36] Woldemar Voigt. *Lehrbuch der kristallphysik:(mit ausschluß der kristalloptik)*, volume 34. BG Teubner, 1910.
- [37] Richard Hill. The elastic behaviour of a crystalline aggregate. *Proceedings of the Physical Society. Section A*, 65(5):349, 1952.
- [38] András Reuß. Berechnung der fließgrenze von mischkristallen auf grund der plastizitätsbedingung für einkristalle. *ZAMM-Journal of Applied Mathematics and Mechanics/Zeitschrift für Angewandte Mathematik und Mechanik*, 9(1):49–58, 1929.
- [39] Junji Awaka, Akira Takashima, Kunimitsu Kataoka, Norihito Kijima, Yasushi Idemoto, and Junji Akimoto. Crystal structure of fast lithium-ion-conducting cubic  $\text{Li}_7\text{La}_3\text{Zr}_2\text{O}_{12}$ . *Chemistry letters*, 40(1):60–62, 2011.
- [40] Tridip Das, Boris V Merinov, Moon Young Yang, and William A Goddard III. Structural, dynamic, and diffusion properties of a  $\text{Li}_6(\text{PS}_4)\text{SCI}$  superionic conductor from molecular dynamics simulations; prediction of a dramatically improved conductor. *Journal of Materials Chemistry A*, 10(30):16319–16327, 2022.
- [41] Walter J Merz. The electric and optical behavior of  $\text{BaTiO}_3$  single-domain crystals. *Physical Review*, 76(8):1221, 1949.
- [42] Lorenzo Gigli, Max Veit, Michele Kotiuga, Giovanni Pizzi, Nicola Marzari, and Michele Ceriotti. Thermodynamics and dielectric response of  $\text{BaTiO}_3$  by data-driven modeling. *npj Computational Materials*, 8(1):209, 2022.
- [43] W Zhong, David Vanderbilt, and KM Rabe. First-principles theory of ferroelectric phase transitions for perovskites: The case of  $\text{BaTiO}_3$ . *Physical Review B*, 52(9):6301, 1995.
- [44] Shenglong Zhang, Tianhao Fei, Tao Cheng, Jia-Yue Yang, and Linhua Liu. Temperature-dependent UV-Vis dielectric functions of  $\text{BaTiO}_3$  across ferroelectric-paraelectric phase transition. *Optics Express*, 31(8):12357–12366, 2023.
- [45] Yubo Qi, Shi Liu, Ilya Grinberg, and Andrew M Rappe. Atomistic description for temperature-driven phase transitions in  $\text{BaTiO}_3$ . *Physical Review B*, 94(13):134308, 2016.
- [46] S Tinte, M G Stachiotti, M Sepiarsky, R L Migoni, and C O Rodriguez. Atomistic modelling of  $\text{BaTiO}_3$  based on first-principles calculations. *Journal of Physics: Condensed Matter*, 11(48):9679, dec 1999.
- [47] Xinjian Ouyang, Yuan Zhuang, Jiale Zhang, Feng Zhang, Xiao Jie, Weijia Chen, Yanxing Zhang, Laijun Liu, and Dawei Wang. Quantum-accurate modeling of ferroelectric phase transition in perovskites from message-passing neural networks. *The Journal of Physical Chemistry C*, 127(42):20890–20902, 2023.
- [48] Yueliang Li, Rong Yu, Huihua Zhou, Zhiying Cheng, Xiaohui Wang, Longtu Li, and Jing Zhu. Direct observation of thickness dependence of ferroelectricity in freestanding  $\text{BaTiO}_3$  thin film. *Journal of the American Ceramic Society*, 98(9):2710–2712, 2015.
- [49] YS Kim, JY Jo, DJ Kim, YJ Chang, JH Lee, TW Noh, TK Song, J-G Yoon, J-S Chung, SI Baik, et al. Ferroelectric properties of  $\text{SrRuO}_3/\text{BaTiO}_3/\text{SrRuO}_3$  ultrathin film capacitors free from passive layers. *Applied physics letters*, 88(7), 2006.
- [50] JY Jo, YS Kim, TW Noh, Jong-Gul Yoon, and TK Song. Coercive fields in ultrathin  $\text{BaTiO}_3$  capacitors. *Applied physics letters*, 89(23), 2006.
- [51] Takeshi Nishimatsu, Umesh V Waghmare, Yoshiyuki Kawa-

- zoe, and David Vanderbilt. Fast molecular-dynamics simulation for ferroelectric thin-film capacitors using a first-principles effective Hamiltonian. *Physical Review B—Condensed Matter and Materials Physics*, 78(10):104104, 2008.
- [52] W Zhong and David Vanderbilt. Effect of quantum fluctuations on structural phase transitions in SrTiO<sub>3</sub> and BaTiO<sub>3</sub>. *Physical Review B*, 53(9):5047, 1996.
- [53] Jingtong Zhang, Louis Bastogne, Xu He, Gang Tang, Yajun Zhang, Philippe Ghosez, and Jie Wang. Structural phase transitions and dielectric properties of BaTiO<sub>3</sub> from a second-principles method. *Physical Review B*, 108(13):134117, 2023.
- [54] Dooman Akbarian, Dundar E Yilmaz, Ye Cao, Panchapakesan Ganesh, Ismaila Dabo, Jason Munro, Renee Van Ginhoven, and Adri CT Van Duin. Understanding the influence of defects and surface chemistry on ferroelectric switching: a ReaxFF investigation of BaTiO<sub>3</sub>. *Physical Chemistry Chemical Physics*, 21(33):18240–18249, 2019.
- [55] GA Samara. Pressure and temperature dependences of the dielectric properties of the perovskites BaTiO<sub>3</sub> and SrTiO<sub>3</sub>. *Physical Review*, 151(2):378, 1966.
- [56] Noriaki Kamaya, Kenji Homma, Yuichiro Yamakawa, Masaaki Hirayama, Ryoji Kanno, Masao Yonemura, Takashi Kamiyama, Yuki Kato, Shigenori Hama, Koji Kawamoto, et al. A lithium superionic conductor. *Nature materials*, 10(9):682–686, 2011.
- [57] Fuminori Mizuno, Akitoshi Hayashi, Kiyoharu Tadanaga, and Masahiro Tatsumisago. New, highly ion-conductive crystals precipitated from Li<sub>2</sub>S-P<sub>2</sub>S<sub>5</sub> glasses. *Advanced Materials (Weinheim)*, 17, 2005.
- [58] Shuting Luo, Xinyu Liu, Xiao Zhang, Xuefeng Wang, Zhenyu Wang, Yufeng Zhang, Haidong Wang, Weigang Ma, Lingyun Zhu, and Xing Zhang. Nanostructure of the interphase layer between a single Li dendrite and sulfide electrolyte in all-solid-state Li batteries. *ACS Energy Letters*, 7(9):3064–3071, 2022.
- [59] Kevin N Wood, K Xerxes Steirer, Simon E Hafner, Chunmei Ban, Shriram Santhanagopalan, Se-Hee Lee, and Glenn Teeter. Operando X-ray photoelectron spectroscopy of solid electrolyte interphase formation and evolution in Li<sub>2</sub>S-P<sub>2</sub>S<sub>5</sub> solid-state electrolytes. *Nature communications*, 9(1):2490, 2018.
- [60] Tao Cheng, Boris V Merinov, Sergey Morozov, and William A Goddard III. Quantum mechanics reactive dynamics study of solid Li-electrode/Li<sub>6</sub>PS<sub>4</sub>Cl-electrolyte interface. *ACS Energy Letters*, 2(6):1454–1459, 2017.
- [61] N. D. Lepley, N. A. W. Holzwarth, and Yaojun A. Du. Structures, Li<sup>+</sup> mobilities, and interfacial properties of solid electrolytes Li<sub>3</sub>PS<sub>4</sub> and Li<sub>3</sub>PO<sub>4</sub> from first principles. *Phys. Rev. B*, 88:104103, Sep 2013.
- [62] Fucheng Ren, Yuqi Wu, Wenhua Zuo, Wengao Zhao, Siyuan Pan, Hongxin Lin, Haichuan Yu, Jing Lin, Min Lin, Xiayin Yao, et al. Visualizing the SEI formation between lithium metal and solid-state electrolyte. *Energy & Environmental Science*, 17(8):2743–2752, 2024.
- [63] Zengcai Liu, Wujun Fu, E Andrew Payzant, Xiang Yu, Zili Wu, Nancy J Dudney, Jim Kiggans, Kunlun Hong, Adam J Rondinone, and Chengdu Liang. Anomalous high ionic conductivity of nanoporous β-Li<sub>3</sub>PS<sub>4</sub>. *Journal of the American Chemical Society*, 135(3):975–978, 2013.
- [64] Naiara Leticia Marana, Silvia Casassa, Mauro Francesco Sgroi, Lorenzo Maschio, Fabrizio Silveri, Maddalena D’Amore, and Anna Maria Ferrari. Stability and formation of the Li<sub>3</sub>PS<sub>4</sub>/Li, Li<sub>3</sub>PS<sub>4</sub>/Li<sub>2</sub>S, and Li<sub>2</sub>S/Li interfaces: A theoretical study. *Langmuir*, 39(51):18797–18806, 2023. PMID: 38079509.
- [65] William D Richards, Lincoln J Miara, Yan Wang, Jae Chul Kim, and Gerbrand Ceder. Interface stability in solid-state batteries. *Chemistry of Materials*, 28(1):266–273, 2016.
- [66] Yizhou Zhu, Xingfeng He, and Yifei Mo. Origin of outstanding stability in the lithium solid electrolyte materials: insights from thermodynamic analyses based on first-principles calculations. *ACS applied materials & interfaces*, 7(42):23685–23693, 2015.
- [67] Zhixiao Liu, Huiqiu Deng, Wangyu Hu, Fei Gao, Shiguo Zhang, Perla B Balbuena, and Partha P Mukherjee. Revealing reaction mechanisms of nanoconfined Li<sub>2</sub>S: implications for lithium–sulfur batteries. *Physical Chemistry Chemical Physics*, 20(17):11713–11721, 2018.
- [68] Sung Chul Jung and Young-Kyu Han. Thermodynamic and kinetic origins of lithiation-induced amorphous-to-crystalline phase transition of phosphorus. *The Journal of Physical Chemistry C*, 119(22):12130–12137, 2015.
- [69] John P Perdew, Kieron Burke, and Matthias Ernzerhof. Generalized gradient approximation made simple. *Physical review letters*, 77(18):3865, 1996.
- [70] Vladimir I Anisimov, Jan Zaanen, and Ole K Andersen. Band theory and Mott insulators: Hubbard U instead of Stoner I. *Physical Review B*, 44(3):943, 1991.
- [71] Amanda Wang, Ryan Kingsbury, Matthew McDermott, Matthew Horton, Anubhav Jain, Shyue Ping Ong, Shyam Dwaraknath, and Kristin A Persson. A framework for quantifying uncertainty in DFT energy corrections. *Scientific reports*, 11(1):15496, 2021.
- [72] Roy Frostig, Matthew James Johnson, and Chris Leary. Compiling machine learning programs via high-level tracing. *Systems for Machine Learning*, 4(9), 2018.
- [73] Ask Hjorth Larsen, Jens Jørgen Mortensen, Jakob Blomqvist, Ivano E Castelli, Rune Christensen, Marcin Dułak, Jesper Friis, Michael N Groves, Bjørk Hammer, Cory Hargus, et al. The atomic simulation environment—a Python library for working with atoms. *Journal of Physics: Condensed Matter*, 29(27):273002, 2017.
- [74] Dong C Liu and Jorge Nocedal. On the limited memory BFGS method for large scale optimization. *Mathematical programming*, 45(1):503–528, 1989.
- [75] Shuichi Nosé. A unified formulation of the constant temperature molecular dynamics methods. *The Journal of chemical physics*, 81(1):511–519, 1984.
- [76] William G Hoover. Canonical dynamics: Equilibrium phase-space distributions. *Physical review A*, 31(3):1695, 1985.
- [77] Michele Parrinello and Aneesur Rahman. Crystal structure and pair potentials: A molecular-dynamics study. *Physical review letters*, 45(14):1196, 1980.
- [78] Michele Parrinello and Aneesur Rahman. Polymorphic transitions in single crystals: A new molecular dynamics method.

*Journal of Applied physics*, 52(12):7182–7190, 1981.

- [79] Samuel Schoenholz and Ekin Dogus Cubuk. Jax md: a framework for differentiable physics. *Advances in Neural Information Processing Systems*, 33:11428–11441, 2020.

## **Acknowledgments**

We gratefully acknowledge the financial support from the RGC General Research Fund (Grant No. 17309620), Hong Kong Quantum AI Lab Limited, Air @ InnoHK of Hong Kong Government, Seed Fund for Basic Research for New Staff 2022/23 (University Research Committee of the University of Hong Kong, No. 2201101550), the Guangdong Shenzhen Joint Key Fund (Grant No. 2019B1515120045) and the National Natural Science Foundation of China (Grant No. 22073007).